THE JOURNAL OF PHYSICAL CHEMISTRY C
A JOURNAL OF THE AMERICAN CHEMICAL SOCIETY

pubs.acs.org/JPCC Article

Phase Stability of Large-Size Nanoparticle Alloy Catalysts at Ab Initio Quality Using a Nearsighted Force-Training Approach

Cheng Zeng, Sushree Jagriti Sahoo, Andrew J. Medford, and Andrew A. Peterson*

Cite This: https://doi.org/10.1021/acs.jpcc.3c04639 Read Online

ABSTRACT: Co−Pt alloyed catalyst particles are integral to commercial fuel cells, and alloyed nanoparticles are important in many applications. Such systems are prohibitive to fully characterize with electronic structure calculations due to their relatively large sizes of hundreds to thousands of atoms per simulation, the huge configurational space, and the added expense of spin-polarized calculations. Machine-learned potentials offer a scalable solution; however, such potentials are reliable only if representative training data can be employed, which typically also requires large electronic structure calculations. Here, we use the nearsighted-force training approach that allows us to make high-fidelity machine-learned predictions on large nanoparticles with >5000 atoms using only small and systematically generated training structures ranging from 38 to 168 atoms. The resulting ensemble model shows good accuracy and transferability in describing the relative energetics for Co−Pt nanoparticles with various shapes, sizes, and Co compositions. It is found that the fcc(100) surface is more likely to form an $L1_0$ ordered structure than the fcc(111) surface. The energy convex hull of a 147-atom icosahedron shows that the most stable particles have Pt-rich skins and Co-rich underlayers and is in quantitative agreement with one constructed by brute-force first-principles calculations. Although the truncated octahedron is the most stable shape across all studied sizes of Pt nanoparticles, a crossover to the icosahedron exists for CoPt nanoparticle alloys due to a large downshift of surface energy. The downshift can be attributed to strain release on the icosahedral surface due to Co alloying. We introduced a simple empirical model to describe the role of Co alloying in the crossover for Co−Pt nanoparticles. With Metropolis Monte Carlo simulations, we additionally searched for the most stable atomic arrangement for a truncated octahedron with equal Pt and Co compositions, and also we studied its order−disorder phase transition. We validated the most stable configurations with a new highly scalable density functional theory code called SPARC. From the outermost shell to the center of a large Co−Pt truncated octahedron, the atomic arrangement follows a pattern: Pt → Co → $L1_2(Pt_3Co)$ → $L1_2(PtCo_3)$ → $L1_0(PtCo)$ → ··· → $L1_0(PtCo)$. Lastly, the order−disorder phase transition for a Co−Pt nanoparticle exhibits a lower transition temperature and a smoother transition compared to the bulk Co−Pt alloy.

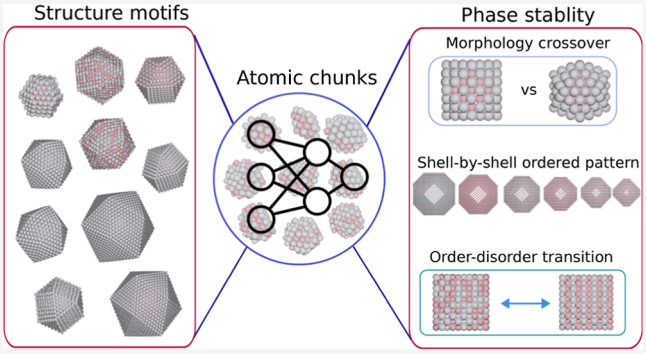

1. INTRODUCTION

Bimetallic nanostructures have received increasing attention in the past two decades.[1−3] Among the family of bimetallic nanostructures, Co−Pt nanoparticles have a wide range of applications in heterogeneous catalysis and magnetic storage.[4−7] Co−Pt nanoparticles have been commercialized as electrocatalysts in fuel-cell electric vehicles such as the Toyoto Mirai.[8,9]

The size, composition, shape, and orderliness of Co−Pt nanoparticles all play a pivotal role in controlling the structure and hence the chemical and physical properties, including the catalytic activity. We provide several examples below and note they are not all in agreement with one another. For example, Li et al. have shown that a core−shell Co−Pt nanoparticle with an ordered core loses fewer Co atoms in electrocatalysis applications than that with a random core.[4] Others have shown that the magnetic and optical properties are closely associated with the orderliness of the structure.[10,11] Yang et al. suggested, based on Monte Carlo simulations, that disordering is initiated at the surface due to the reduced coordination, hence lowering the ordering temperature.[12] Müller and Albe pointed out that surface segregation of one element can have a large impact on the ordering.[13] Alloyeau et al. showed in both experiments and simulations that the shape and size affect the order−disorder transition, indicating that a larger nanoparticle tends to show a higher transition temperature and the size effect is uniquely determined by the smallest length of a nano-

Received: August 4, 2023
Revised: October 16, 2023
Accepted: November 6, 2023

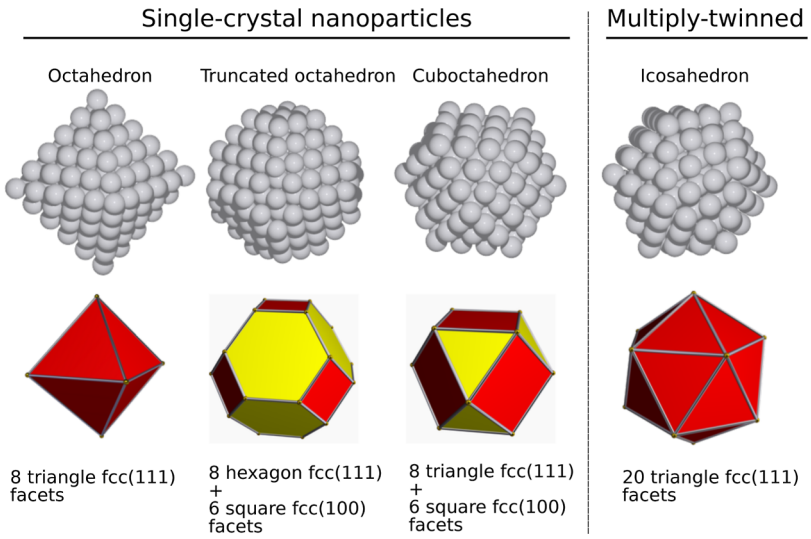

Figure 1. Atomic configurations and geometrical shapes of nanoparticles in various shapes.

particle.[14] Alloyeau's large-scale simulation was based on tight-binding potentials fitted to experimental and first-principles calculations, and the most stable structure for an equal-composition nanoparticle was identified to be a fully $L1_0$ ordered truncated octahedron.[14] However, first-principles calculations by Gruner et al.[53] suggested that the most stable shape of a Co−Pt nanoparticle at small sizes is not the $L1_0$ ordered regular truncated octahedron but a multiply twinned icosahedron.

Pure Pt nanoparticles are normally stable in the single crystal structure, whereas Pt alloy nanoparticles can exist in multiply twinned structures such as an icosahedron,[15−18] although the shape of Pt nanoparticles can be controlled by capping materials.[19] It is thus crucial to understand the characteristics of structure motifs, such as the icosahedron and octahedron. An icosahedron is created by packing 20 tetrahedra in a manner that they share a common vertex, leading to close-packed surfaces, but distorted tetrahedra (see Figure 1). This distortion leads to a high internal strain with a relatively low surface energy.[20] Thus, icosahedra are normally more stable at small sizes, where the surface energy prevails over the volume contribution.[21]

In contrast, an octahedron structure preserves the bulk lattice symmetry—it can be obtained by directly cutting a single crystal. The normal octahedron only has fcc(111) facets and has no internal strain. To lower the total energy, the six "tips" of the octahedra can be removed, creating a truncated octahedron[22] (Figure 1). Although this raises the energy per surface area by creating six fcc(100) facets, it lowers the total amount of surface area, which suggests it may be more stable at larger sizes.[23] The cuboctahedron can be conceptualized in a similar way: starting with a cube with six fcc(100) facets, the eight corners are cut off, exposing eight new triangular fcc(111) facets (Figure 1).

The trade-off between surface and volume contributions lead to possible crossovers in stability among structural motifs as the particle size changes; for pure nanoparticles, past researchers have used simple empirical thermodynamic models to describe this phenomenon.[22−25] In the case of bimetallic nanoparticles, crossovers among various shapes have rarely been reported. For the related case of Pd−Au particles, Zhu et al. used an empirical model fit to density functional theory (DFT) calculated properties to show that alloying of Pd can extend the stability of icosahedron Pd−Au nanoparticles beyond that of pure Au nanoparticles because of the stress release when two different metals are mixed.[26] Since the empirical potential was fit to a small number of properties, the prediction accuracy over a large range of different nanoparticle structures is uncertain. We are not aware of any crossover studies directly addressing Co−Pt nanoparticles.

The crossovers in bimetallic nanoparticles are not likely to be fully understood without reliable descriptions of the atomic interactions. In an ideal world, such studies would employ electronic structure calculations directly. DFT offers a good compromise between accuracy and computational cost. However, model systems of practically sized nanoparticles, with sizes of 1000−10,000 atoms, are notoriously expensive for even single calculations, due to the famous $O(N^3)$ scaling, where N indicates the system scale, such as the number of electrons, number of atoms or number of basis functions. For nanoparticle structure exploration, the picture is more grim due to the huge combinatorial space that must be explored to describe the range of sizes, crystal structures, facets, and alloy (dis)ordering that may be encountered. Further, as a magnetic system, Co−Pt particles have an added expense in electronic structure due to the requirement for spin-polarized calculations. These combinations of factors make the rigorous exploration of the Co−Pt structure−function relationship out of reach for methods like DFT.

Machine-learned interatomic potentials have gained momentum in fitting potential energy surfaces calculated by ab initio calculations.[27−33] However, a fundamental problem arises in using atomistic machine learning to perform large-scale simulations: for high-fidelity potentials, the training data should closely resemble the ultimate structures being predicted and the generation of such training data for nanoparticles can be very costly, as described above. To circumvent this issue, we recently released a "nearsighted force-training" (NFT)[34] approach to generate small-size training data to systematically learn the forces and energies of large structures. In this approach, a bootstrap ensemble[35] (or any other reasonable uncertainty metric) is used to identify the most uncertain atoms in a particular structure. Atomic "chunks" centered on these uncertain atoms are removed and calculated at large enough size that the central atom's force can be calculated with fidelity by DFT. Only the force on the central atom is used in the loss

https://doi.org/10.1021/acs.jpcc.3c04639
J. Phys. Chem. C XXXX, XXX, XXX−XXX

function, thus adding targeted data and avoiding noise associated with boundary atoms. We demonstrated that this approach successfully built and relaxed nanoparticles containing up to 1415 atoms in previous work.

Here we apply the NFT approach to build a robust ensemble model for Co−Pt nanoparticles. Using these well-validated neural network models, we optimize the structures of Co−Pt alloys of simple bulk, fcc(111) surfaces, fcc(100) surfaces, and icosahedron and octahedron nanoparticles of various sizes and compositions. Moreover, we aim to address a number of key problems regarding the thermodynamic stability of Co−Pt nanoparticles, including the crossover among Pt and Co−Pt structure motifs, the most stable atomic arrangement of a Co−Pt truncated octahedron, and the order−disorder phase transition of Co−Pt truncated octahedron.

2. METHODS

2.1. Model Creation with Nearsighted Force Training. We used the nearsighted-force training (NFT) approach[34] to generate the machine-learning model without the need for large-sized training data, which is expensive to obtain. In this method, we started with a small training set consisting of 18 Co−Pt bulk structures calculated in density functional theory (DFT), sampled following the initialization procedure we previously described.[34] We trained a bootstrap ensemble[35] of Behler−Parinello-type machine-learning models to this minimal training set; details of the model parameters are described later. When this ensemble model is applied to a new structure, it gives a systematic estimate of the uncertainty of each atom in that structure.

We started the NFT active-learning procedure on a "rattled" $Pt_{192}Co_{68}$ cuboctahedron, that is, we used the ensemble to identify the most uncertain atom in the structure, and then we pulled out a "chunk" of this atom and its neighbors within a cutoff distance of 8 Å. This chunk was calculated in DFT, and solely the force on the central atom was added to the training set. The ensemble was restrained, and the procedure was repeated on the next most uncertain atom. We terminated this process after 9 NFT steps because the uncertainty did not improve in two consecutive steps, and we wanted our model to be optimized for low-force structures.

Next we performed a relaxation on this structure and used the NFT model to extract uncertain chunks along the relaxation trajectory, with the procedure we described earlier,[34] leading to a systematic improvement of the description of this relaxed particle. We generally stopped the active learning process when any of three criteria were met: the uncertainty was below the convergence criterion, the number of retraining steps exceeded a predefined number, or the target uncertainty was not lowered for two continuous steps.

After we completed the NFT procedure on the $Pt_{192}Co_{68}$ particle, we continued to improve our model by training on a variety of octahedral and icosahedral nanoparticles, allowing us to find atomic chunks representing diverse local chemical environments that are unique and informative for potential energy surfaces of Co−Pt nanoparticles. The icosahedron nanoparticles include Pt_{1415}, fully disordered $Pt_{736}Co_{679}$, a CoPt/2Pt core−shell with a disordered core ($Pt_{1150}Co_{265}$), a CoPt/1Pt core−shell with a disordered core ($Pt_{3092}Co_{1991}$), and a CoPt/2Pt core−shell with a disordered core ($Pt_{3694}Co_{1389}$). The cuboctahedron nanoparticles include $Pt_{192}Co_{68}$ with a disordered core, a Pt_{1415}, a core−shell CoPt/Pt cluster $Pt_{975}Co_{440}$ with a disordered core, a fully $L1_0$ ordered Co−Pt cluster $Pt_{736}Co_{679}$, and a fully disordered Co−Pt cluster $Pt_{736}Co_{679}$. In total, 2064 atomic "chunks" in sizes from 38 to 168 atoms were extracted from those nanoparticles. Adding the 18 bulk cells, we had a total of 2082 training images. By building the training set in this manner—as opposed to relying on human intuition, where similar structures are designed by hand—we can be confident that our training set is specialized to the structures of interest to this study.

The statistics of these 2064 generated atomic chunks are discussed in the Supporting Information, including the distributions of forces on the central atom, number of atoms, force prediction residuals, and energy prediction residuals. The nanoparticle trajectories, training images (atomic chunks), force, and energy ensemble models are included as Supporting Information sets.

2.2. Model Structure. We took a bootstrap approach[35] to sample the training images for each neural network model, and our ensemble consisted of 10 neural network models. Ensemble averages were used as the predictions for both the energy and forces. Atomic uncertainties were proportional to standard deviations of the ensemble force predictions, as used in Zeng et al.[34] Each member of neural network models is a Behler−Parrinello type.[27] Neural network models were constructed using an open-source atomistic machine learning package (AMP) developed in our group.[36] Fast force and energy inferences were carried out with n2p2, which is mainly developed by Singraber et al.[37] Fast fingerprinting was performed with SIMPLE-NN implemented with AmpTorch.[38,39] Gaussian symmetry functions with a cutoff radius of 6.5 Å were used to encode the local chemical environments. For the feature vector of Co elements, it consists of 12 G2 and 8 G4 symmetry functions, where the Pt feature vector comprises 13 G2 and 7 G4 symmetry functions. Full details of the symmetry functions are included in the Supporting Information set in the JSON format. 3000 epochs were used for training. A simple structure of (20, 5, 5, 1) was employed for the neural network topology to mitigate overfitting. A L_2 regularization ($L_2 = 0.001$) was used to avoid large atomic neural network weights, hence alleviating the overfitting. To avoid the challenges of creating a model that can produce consistent force and energy predictions over wide regions of configuration space, we trained both a force ensemble model and an energy ensemble model on our 2082 images, referred to hereafter as the force model and energy model, respectively. This was done in order to allow our model sizes to be smaller and our training procedures to be faster with each individual model optimized for its own prediction of interest. The force model was trained on the forces of central atoms of atomic chunks and on both energy and forces of bulk cells. The energy model was trained on the total energies of the bulk cells and atomic chunks.

2.3. Electronic Structure Calculations. DFT calculations for bulk, atomic chunks and 201-atom nanoparticles were carried out with the GPAW code.[40] The Perdew−Burke−Ernzerhof (PBE) exchange−correlation functional with a plane wave cutoff of 350 eV was used.[41] To achieve a fast convergence, a Fermi−Dirac smearing of 0.1 eV was utilized, and the energetics were extrapolated to 0 K. Calculations for atomic chunks were sampled at the Γ-point of the Brillouin zone, where calculations for bulk cells used a k-point grid of $12 \times 12 \times 12$. For atomic structures, including cobalt, spin polarization was included. When only platinum was present, the calculations were spin-paired. The lattice constant of bulk Pt was found to be 3.936 Å. Atomic chunks were placed in a nonperiodic box where

https://doi.org/10.1021/acs.jpcc.3c04639
J. Phys. Chem. C XXXX, XXX, XXX−XXX

the shortest distance to the box wall is at least 5 Å. Self-consistent field (SCF) calculations were considered to be converged when the energy difference between the last three steps is less than 0.0001 eV/electron. Structure optimizations used an MDMin algorithm until the maximum atomic force was not larger than 0.05 eV/Å.

DFT calculations of the 586-atom particles were done using the highly parallel "Simulation Package for Ab-initio Real-space Calculations" (SPARC) code.[42−44] To the best of our knowledge, this calculation represents the largest size of Co−Pt nanoparticles that has ever been studied directly with DFT. A mesh spacing of 0.13 Å (0.25 bohr radii) was used in a Γ-point calculation with the PBE functional and the PseudoDojo pseudopotentials,[45] and all calculations were run until the energy converged to within 2.7×10^{-4} eV/atom (1×10^{-5} Ha/atom). Atomic forces were computed and compared with GPAW results for smaller systems, which showed that the mean absolute force error between the codes is below 0.025 eV/Å for all systems tested (see Figure S3 in the Supporting Information). Particles were surrounded by 3.5 Å of vacuum in each direction with Dirichlet boundary conditions in all directions.

Note that unlike our prior publication,[34] in this work, we dealt with a magnetic system. The underlying assumption for NFT to be applicable for magnetic systems is that in the electronic ground state, there exists a unique mapping from atomic positions to spin states (or magnetic moments), which also display a strong locality. In general, forces may depend on the initial guess of magnetic moments since a poor initial guess may lead to a different local-minimum spin configuration. Thus, we have used a consistent initial-guess strategy for all calculations, with an initial magnetic moment of 0 μ_B for Pt atoms and 2.1 μ_B for Co atoms.

2.4. Global Optimization Techniques. We aimed to explore a wide range of potential energy surfaces with an emphasis on structures of nanoparticles in various shapes. We were particularly interested in the global minima for a given shape, size, and alloy composition. However, searching global minima by using a brute-force approach is computationally prohibitive. For example, if we consider a small fixed-shape 147-atom nanoparticle with 73 Co and 74 Pt atoms, the number of possible atomic arrangements is already as large as $147!/(73! \times 74!) \approx 10^{44}$. Although symmetry can reduce the complexity, attempting to exhaust the search space is inaccessible even with machine-learned potentials, especially for large nanoparticles of thousands of atoms. Instead, we used global optimization techniques, specifically genetic algorithms and Metropolis Monte Carlo simulations.

2.4.1. Genetic Algorithms. Genetic algorithms, inspired from evolutionary theory, have become popular in the past two decades for optimizing structures.[46−50] The genetic algorithm was performed on both Co−Pt surfaces and a type of Co−Pt icosahedron to construct energy convex hulls. The genetic algorithm was set up with the Atomic Simulation Environment (ASE)[51] based on the procedure implemented by Lysgaard et al.[49] and Van den Bossche et al.[50] We used a rigid structure; that is, all derived structures are not allowed to relax. Structural relaxation was performed afterward if needed. To make comparisons between different compositions, we define the negation of the mixing energy $E_f(Pt_xCo_y)$ of a structure Pt_xCo_y as the fitness score to propagate the algorithm

$$E_f(Pt_xCo_y) = E(Pt_xCo_y) - \frac{x}{x+y}E(Pt_{x+y}) - \frac{y}{x+y}E(Co_{x+y}) \quad (1)$$

where $E(Pt_xCo_y)$, $E(Pt_{x+y})$, and $E(Co_{x+y})$ denote the ML model calculated per-atom energies of the corresponding structures. We first studied the fcc(111) and fcc(100) surfaces. For the fcc(111) and fcc(100) surfaces, we used a 4 × 4 × 5 supercell with a size of 80 atoms with 13 Å separation between slabs in the direction orthogonal to the surface. The initial generation was populated with 120 surfaces by using randomly chosen compositions. The lattice constants of pure Co and Pt slabs were determined by the force model, and for the mixed slabs, the lattice constant is linearly interpolated based on Vegard's law. We used three ASE operators to create the next generation. "CutSpliceCrossover", as introduced by Deaven and Ho,[46] takes two parent structures, then cuts them in a random plane, and combine the halves from two parent slabs together to form an offspring. The second operator "RandomSlabPermutation" was used to randomly permute two atoms of different types. The last "RandomCompositionMutation" changes the composition of the slab by mutating one element to the other. The probability of the above three operators are, respectively, 0.6, 0.2, and 0.2. In addition, we used a variable function named "RankFitnessPopulation" to uphold the composition diversity at each generation so that optimization is performed on a full range of compositions. We ran the experiments for 100 generations.

This approach was also used to build the convex hull of a 147-atom Co−Pt icosahedron nanoparticle. The initial generation was populated with 100 members, the composition was randomly chosen, and the lattice constant was obtained by linear interpolation. For the icosahedron nanoparticle, we were interested in the fittest Co/Pt composition; hence, we did not restrict the algorithm to keep a wide range of compositions in each generation. For the nanoparticles, four types of operations were utilized to create the offspring, including "CutSpliceCrossover", "RandomSlabPermutation", "MirrorMutation" (to mirror half of the cluster in a randomly oriented cutting plane while discarding the other half), and "SymmetricSubstitue" (to permute all atoms within a shell of the symmetric particle), and the corresponding operation probabilities are 3/6, 1/6, 1/6, and 1/6, respectively. This experiment was also run for 100 generations. After the runs were completed, we chose to study structures after the 80th generation. We pinpointed the Co−Pt icosahedron with the most negative formation energy, which is named the fittest Co−Pt icosahedron. We calculated the Pt composition of the fittest structure, and we selected structures whose mole fractions of Pt are close to the fittest one based on a Gaussian function. In total, 232 Co−Pt icosahedron nanoparticles were selected, and energetics of their relaxed structures were used to construct the energy convex hull for the 147-atom Co−Pt icosahedra.

2.5. Metropolis Monte Carlo Simulations. Previous works suggested that while a genetic algorithm was more efficient to search a wide range of compositions, Metropolis Monte Carlo simulations were found to be more effective for structures with fixed compositions.[12,13,52] We thus employed such Metropolis calculations in the canonical ensemble. At each elementary Monte Carlo step, two neighboring atoms of different element types were exchanged, and the energy change was calculated for the exchange. The new structure was accepted if the energy change was negative or it is accepted based on the

https://doi.org/10.1021/acs.jpcc.3c04639
J. Phys. Chem. C XXXX, XXX, XXX−XXX

Boltzmann probability if the energy change was positive. The number of Monte Carlo steps was determined in a way that on average, at least 40 swaps were performed for each atom in the structure. We used these simulations at 300 K to find the putative global minima of truncated octahedra $Pt_{96}Co_{105}$ and $Pt_{300}Co_{286}$, and we compared them to the fully $L1_0$ ordered counterpart at full DFT levels of theory. We also used these simulations at temperatures ranging from 300 to 1800 K to study the order−disorder phase transitions for Co−Pt bulk and nanoparticles with nearly equal compositions of Co and Pt. For each Monte Carlo trajectory at a given temperature, the order parameter was calculated as the average over the configurations after a burn-in period.

3. RESULTS AND DISCUSSION

The key objective of this study is to train robust machine learning models that can predict stable structures of nanoparticles, which we will use to distinguish the phase stability of bimetallic nanoparticles with various shapes and atomic arrangements.

3.1. Comparison to Literature Structures and Ab Initio Calculations. We first validated our ML models by a comparison with published ab initio calculations; additional validation calculations are reported in Sections 3.2 and 3.4, and comparisons to literature-reported structures and trends are contained in Sections 3.2, 3.3, and 3.4.

Gruner et al. used first-principles calculations to compare the energetics of several structural motifs of Co−Pt alloy nanoparticles in reference to an $L1_0$ ordered cuboctahedron.[53] We created a number of 561-atom nanoparticles for $Pt_{296}Co_{265}$ that are either identical or close in atomic arrangements to those used in Gruner's ab initio calculations since the exact structure was not always reported. Different randomness should play a negligible role in the energetics because only a small fraction of atoms are randomly positioned. The nanoparticles included an $L1_0$ ordered cuboctahedron, a disordered icosahedron, an icosahedron with alternating Co and Pt shells, and a core−shell icosahedron with a Co-rich second shell. We relaxed these structures with the force model and then we calculated the energetics with the energy model. The comparison between ML predictions and ab initio calculations by Gruner et al. is shown in Figure 2. We note that the work of Gruner et al. used a cutoff (268 eV) that was smaller than the one (350 eV) we used for DFT calculations on atomic chunks, which may account for some discrepancy to the literature. One can see a very good agreement for both cuboctahedron and icosahedron nanoparticles, and the overall order for all structures presented is exactly captured by the ML models, with the mean ensemble prediction agreeing very well and the parity line within the error bars.

In addition, we created a 147-atom Pt icosahedron and cuboctahedron, relaxed it with the ML model, and compared the absolute energy difference to that obtained by the DFT calculations we performed in the GPAW calculator. The DFT and ML-predicted energies for both structures are presented in Figure S4 of Supporting Information. Although the exact energetics for each shape can differ by 13.6−27.2 meV/atom between ML predictions and DFT calculations, the relative energy difference between those two shapes is much closer; Pt icosahedron is more stable than Pt cuboctahedron by 7 meV/atom using ML models versus 8.6 meV/atom using DFT calculations. This suggests that the ML models are able to distinguish the thermodynamic stability across various shapes of nanoparticles and different atomic arrangements for a given shape.

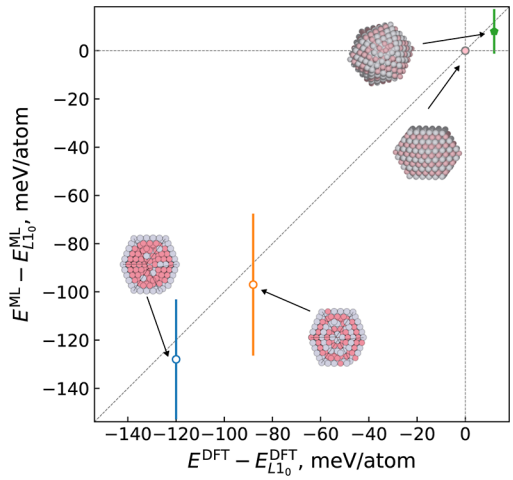

Figure 2. Energetics of $Pt_{296}Co_{265}$ nanoparticles in various shapes in reference to the $L1_0$ ordered cuboctahedron: ML predictions versus DFT calculations by Gruner et al.[53] The DFT calculations used a smaller cutoff (268 eV) compared to 350 eV used to obtain the training data for the ML models. The error bar represents the ensemble halfspread as defined by Peterson et al.[35]

3.2. Energy Convex Hull of Co−Pt Surfaces and Nanoparticles. We next turn to studying the relative stability of alloyed structures by using these potentials to construct "convex hulls" that plot the alloy-formation energy versus composition. Negative energies indicate that the alloy is stable relative to the pure components.

We began by examining the formation energy of two ordered bulk alloys, PtCo and Pt_3Co. The formation energy for PtCo and Pt_3Co are −0.24 and −0.14 eV/atom, respectively, close to values by experiments and empirical potentials.[11,54] As a comparison, the DFT-calculated formation energies for PtCo and Pt_3Co are −0.10 and −0.06 eV/atom, respectively. This indicates that Co and Pt atoms have a strong tendency of being mixed.

To gain insights into the atomic arrangement near a Co−Pt surface, we built energy convex hulls for 5-layer Co−Pt fcc(100) and fcc(111) surfaces using the neural-network-enhanced genetic algorithm. Figure 3a shows the energy convex hull for fcc(100), where x_{Co} represents the mole fraction of the Co atoms. We extracted the fittest fcc(100) surface (that with the lowest formation energy), and its composition is around x_{Co} = 0.4. A side view of the global minima, shown in the figure, implies that it is an $L1_0$ ordered structure, forming alternating Pt and Co layers, with the outermost layer being Pt. Although the convex hull of fcc(100) is not symmetric, we can infer that this lack of symmetry is constrained by the number of layers (5), and if it were increased, it would approach a more symmetric form. The structure at x_{Co} = 0.2 is close to $L1_2$ ordered, which suggests that the atomic arrangement in a fcc(100) surface is inclined to form an ordered structure. We anticipate that compositions of stable structures may change if we increase the thickness of the surface where bulk contributions become more dominant (e.g., global minima closer to 0.5 for an infinitely thick surface). Yet atomic arrangement patterns, in particular near surfaces, should hold for thicker surfaces. We will see this to be the case when we examine large nanoparticles.

https://doi.org/10.1021/acs.jpcc.3c04639
J. Phys. Chem. C XXXX, XXX, XXX−XXX

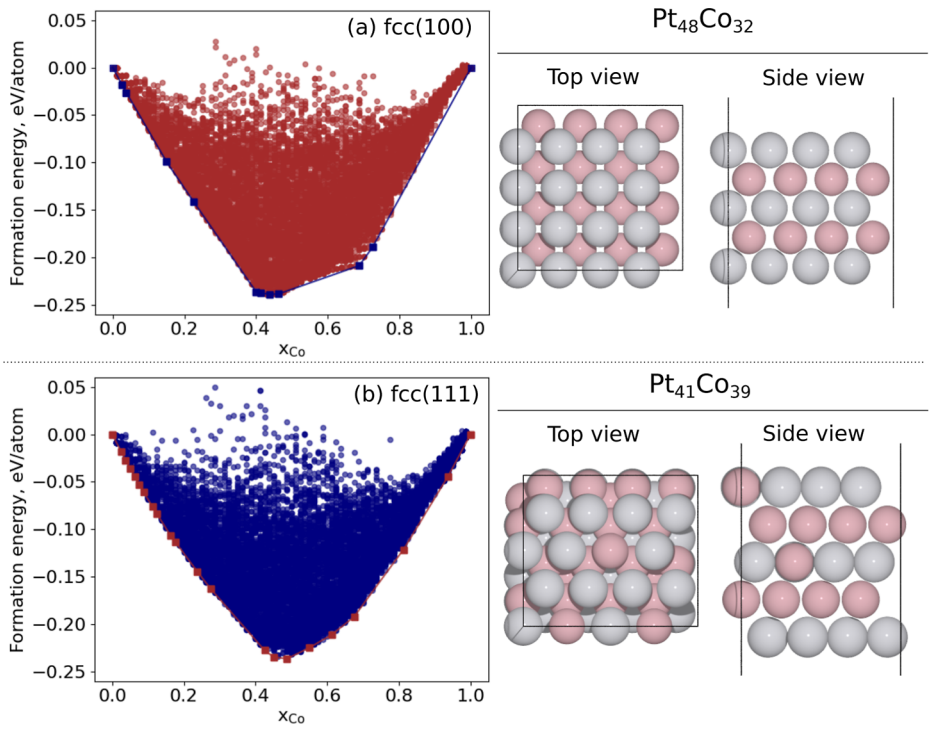

Figure 3. Energy convex hulls of fcc(100) (a) and fcc(111) (b) surface PtCo alloys as a function of Co compositions. Solid squares are the stable structures, and circles refer to unstable structures. Top and side views of the fittest configurations are shown on the right.

In comparison, the convex hull of the fcc(111) surface alloys is much smoother, representing more flexibility in atomic arrangements in this more closely packed facet. In terms of the fittest configuration $Pt_{41}Co_{39}$, the general trend still holds that Pt tends to segregate at the surface while being depleted at the subsurface. A small amount of Co shows up at the surface, although Co−Co direct connections are not present. In brief, the main features of atomic arrangements for both fcc(100) and fcc(111) surfaces are a surface Pt layer and a subsurface Co layer. Besides, the fcc(100) surface is more likely to form an ordered structure than the fcc(111) surface.

Next, we turned to building the convex hull of a 147-atom Co−Pt icosahedron. Figure 4 shows the formation energy for this system as a function of the mole fractions of Co atoms, centered on the Pt-rich region where the global minimum lies. The convex hull from a DFT-based study conducted by Noh et al.[55] is also included for comparison. The trend of formation energy versus composition demonstrates that the ML-predicted convex hull agrees very well with the ab initio results. The prediction discrepancy of the formation energies is less than 0.03 eV/atom across the composition range, as shown in Figure 4. The discrepancy could likely be reduced by adding additional atomic chunks extracted from uncertain 147-atom Co−Pt icosahedra—here, we did not seek such an improvement since we considered the prediction accuracy to be satisfactory. On the Pt-rich side (increasing from $x_{Co} = 0$), the formation energy rapidly decreases with the addition of Co. In contrast, there exists a wide flat region ($0.3 \leq x_{Co} \leq 0.5$) where either the addition or removal of Co atoms barely changes the formation energy.

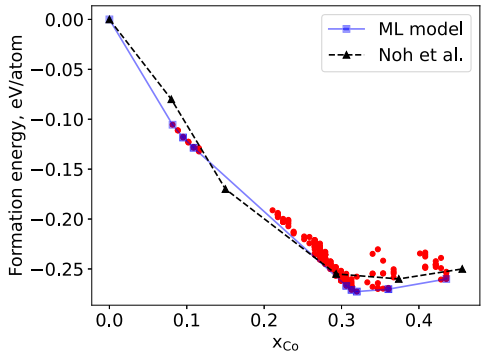

Figure 4. Energy convex hull of a 147-atom Co/Pt Ih as a function of Co compositions. Solid squares are the stable structures found by ML models, and circles refer to unstable structures of ML predictions. Up-triangles refer to the stable structures excerpted from Noh et al.[55]

The most significant feature (also reported by Noh et al.) along the convex hull is the formation of a Pt skin on the surface with a Co-rich layer directly below the Pt skin. Among the eight Co−Pt icosahedra along the hull in Figure 4, seven structures are covered by a full Pt skin, with the exception being the one with the lowest overall platinum composition ($x_{Co} = 0.44$), where the skin contains 78% Pt. The average Co composition of the second shell is 74%.

It is well-known in fuel-cell catalysis that Pt−Co alloyed catalysts exhibit a platinum skin, which is generally considered to be formed by dealloying of the cobalt under electrochemical conditions, due to the difference in electrodeposition potential between Co and Pt. The Pt skin is contracted relative to what would be found on a pure-Pt particle, which has been concluded to increase the catalyst's activity. These results show that Pt is also thermodynamically most stable on the surface (for a fixed Pt/Co composition). This may suggest a greater long-term stability to these catalysts than if the skin layer were present due to cobalt dissolution alone.

On the left side of the convex hull, the ML model identifies a stable structure with the composition $Pt_{83}Co_{64}$, where Co atoms on the surface occupy the center of fcc(111) surfaces. In this

https://doi.org/10.1021/acs.jpcc.3c04639
J. Phys. Chem. C XXXX, XXX, XXX−XXX

same region, Noh et al.'s calculations show a structure with the composition $Pt_{80}Co_{67}$, where Co atoms on the surface sit at the corners. To validate whether the center occupancy represents a stable atomic arrangement, we constructed icosahedron structures with stoichiometry $Pt_{80}Co_{67}$ where surface Co atoms occupy both types of sites and compared the energies with both DFT and ML calculators. In both cases, the corner occupancy was predicted to be more favorable, with DFT energies showing a difference of ∼14 meV/atom, which indicates that the terrace center occupancy is a low-energy state as well. However, this configuration was not captured in the DFT calculations by Noh et al.[55] The configurations of two types of $Pt_{80}Co_{67}$, together with their ML and DFT energies, are provided in Figure S5 of Supporting Information. Since both calculators correctly show the corner site to have lower energy, this indicates that the two procedures captured different minima structures purely by the stochasticity of the genetic algorithm itself and not due to an issue with the ML fidelity.

3.3. Crossovers among Morphology in Pt and Co−Pt Nanoparticles.

3.3.1. Platinum Particles. In this section, we aim to provide physical insights into the distinct crossover behavior of Co−Pt nanoparticles. We first focus on pure Pt nanoparticles, where the crossover between different shapes has been extensively investigated based on well-parametrized empirical potentials.[22,23,56] The energies of each structure in such studies were fit to an empirical thermodynamic model, dividing the total potential energy (U) for a nanoparticle of a specific shape into contributions from volume, surface, and edges

$$\frac{U}{N} = A + BN^{-1/3} + CN^{-2/3} \tag{2}$$

where N is the total number of atoms, and A, B, and C are parameters corresponding to the volume, surface, and edge contributions, respectively. These parameters are unique to each nanoparticle shape. As N increases, the edge contribution becomes less important, and we will show that this term can be dropped in the size range of interest.

Discrepancy exists in the literature, even for the crossover of pure Pt nanoparticles. For example, Uppenbrink and Wales concluded that the crossover between icosahedron and decahedron occurs at around 393 atoms for both pure Pt and pure Au nanoparticles, a decahedron is found in a narrow range of sizes and decahedron becomes less stable than cuboctahedron at a size of 550 atoms.[22] In contrast, Baletto et al., using a different empirical potential and a metric defined as bulk modulus divided by cohesive energy, concluded that the crossover between icosahedron and decahedron should occur in a small size (<100 atoms), decahedra can exist in a wider range of sizes and truncated octahedron becomes dominant at around 6500 atoms.[23] For simulations on small-size Pt nanoparticles, either cuboctahedron or regular truncated octahedron has been used in previous works.[14,18,57] Although controlling experimental conditions can open up possibilities for a variety of shapes of pure Pt nanoparticles, it is well acknowledged that multiply twinned structures rarely form.[16]

We used the well-validated ML models to predict energetics of typical structure motifs of Pt nanoparticles across a size range of 201 to 6266 atoms, including seven cuboctahedron, five truncated octahedron, and seven icosahedron nanoparticles; decahedron is not considered because it is usually only an intermediate state and it has been rarely reported in experiments.[16,58] We then fit the predicted energetics of each structure type as a function of N to a simplified version of eq 2 in which we dropped the edge term ($CN^{-2/3}$).

The results are shown in Figure 5, which shows per-atom energy versus $N^{-1/3}$. (Results including edge terms are included

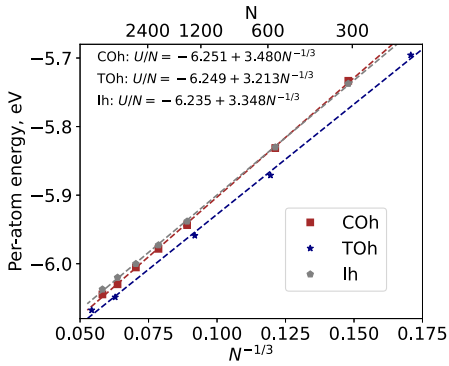

Figure 5. Energies of relaxed structure motifs of Pt nanoparticles, plotted as per-atom energy (U/N) versus $N^{-1/3}$. COh, TOh, and Ih represent cuboctahedron, truncated octahedron, and icosahedron, respectively.

in Figure S6 of Supporting Information). First, we note that the data points show little significant curvature about the straight lines, which implies that the neglect of edge terms is justified for this range of particle size. From the fit parameters displayed on the plot, one can see that volume contributions of single-crystal cuboctahedron and truncated octahedron are almost identical, while that of icosahedron is larger. We attribute this to the distorted internal structure of the icosahedron. As we expect, the surface contribution is always positive, with the order of cuboctahedron > icosahedron > truncated octahedron. It is reasonable that the surface contribution of the cuboctahedron is larger than that of the icosahedron because more fcc(100) facets are exposed on the cuboctahedron surface compared to all fcc(111) facets on the icosahedron surface. It was also found that the surface contribution of truncated octahedron is lower than icosahedron, probably because the distorted internal structure of icosahedron also has a profound impact on its surface energy (i.e., the icosahedron surface may be distorted as well).

This analysis shows the truncated octahedron to be the most stable Pt shape across this size range (roughly 200−7000 atoms). To the best of our knowledge, it is the first time that the unique high stability of truncated octahedron is identified and attributed to the lower surface energy contribution compared to that in icosahedra, and it explains the observation that truncated octahedron is the structure of pure Pt nanoparticles most frequently found in experiments.[16,18] A crossover exists between cuboctahedron and icosahedron, which is estimated to be at N = 538, in agreement with the result of Uppenbrink and Wales.[22] However, these lines are nearly overlapping, which presumably makes the precise location of the crossover very sensitive to the fidelity of the interatomic potential used, perhaps explaining the large variation seen in the literature for the location of this crossover.

3.3.2. Bimetallic Particles. Using a similar logic, we extended this analysis to the crossover in Co−Pt nanoparticles. Section 3.2 concludes that the most outstanding feature for Co−Pt nanoparticles is an outermost Pt skin with a Co-rich second shell. Thus, for truncated octahedron and icosahedron, we created Co−Pt structure motifs enforcing the above feature, with the remaining Co atoms randomly placed in the core. As a

https://doi.org/10.1021/acs.jpcc.3c04639
J. Phys. Chem. C XXXX, XXX, XXX−XXX

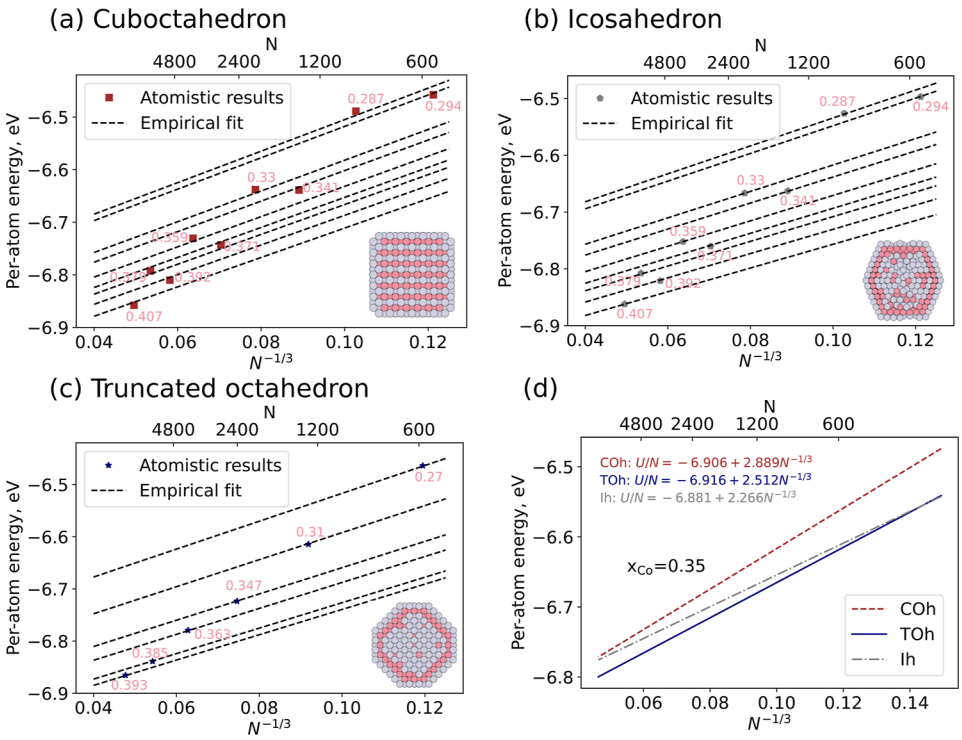

Figure 6. Energies of relaxed structure motifs of Co−Pt nanoparticles, plotted as per-atom energy (U/N) versus $N^{-1/3}$. COh, TOh and Ih represent cuboctahedron, truncated octahedron, and icosahedron, respectively. (a) Cuboctahedron, (b) icosahedron, (c) truncated octahedron, and (d) fitted results using eq 3, at a Co composition of 35%. The Co compositions are indicated by texts next to each data point. The fitted family of lines are indicated by dash lines; each line represents the fit for the fixed Co composition indicated by the nearest point. Cross-sectional view of the structure motif for Co−Pt nanoparticles are included as an inlet. The number of atoms are presented in the twin axis at the top.

Table 1. Fitted Enthalpy of Mixing (α) and Reduction of Pt Surface Energy Due to Co Alloying (κ) for Each Shape of Co−Pt Nanoparticles[a]

	α [eV/atom]	κ [eV/atom$^{4/3}$]	A_{Pt} [eV/atom]	B_0 [eV/atom$^{4/3}$]	A_{Co} [eV/atom]
cuboctahedron	−0.913	0.485	−6.251	3.480	−7.528
icosahedron	−0.850	0.924	−6.235	3.348	−7.528
truncated octahedron	−0.966	0.624	−6.249	3.213	−7.528

[a]Fitted volume (A_{Pt}) and surface contributions (B_0) in a pure Pt nanoparticle are also listed. The volume contribution of Co (A_{Co}) obtained from a bulk calculation is shown as well.

comparison, we also included a cuboctahedron with an $L1_0$-ordered core surrounded by pure Pt skin. To account for the Co composition effect on the energetics, we introduced a revised empirical model, as shown in the following equations. In the interest of having fewer parameters, we assume edge sites can be neglected (as we justified earlier for pure Pt particles in this size range). Our intention is to use the simplest model that captures the trends of interest, to maximize interpretability and minimize overfitting.

$$\frac{U}{N} = A(x_{Co}) + B(x_{Co})\cdot N^{-1/3} \tag{3}$$

where

$$A(x_{Co}) = x_{Co}A_{Co} + (1 - x_{Co})A_{Pt} + \alpha x_{Co}(1 - x_{Co}) \tag{4}$$

and

$$B(x_{Co}) = B_0(1 - \kappa x_{Co}) \tag{5}$$

Here, A_{Pt} and B_0 are respective volume and surface contributions found from pure Pt nanoparticle results. A_{Co} is the volume contribution in a pure Co nanoparticle; this was determined from a bulk calculation. α describes the enthalpy of mixing, and κ describes the reduction of the Pt surface energy due to alloying the bulk with Co; both of these were taken as free variables fit to the Co−Pt particles in question. The ML-calculated energetics for the cuboctahedron, icosahedron, and truncated octahedron are shown in Figure 6a−c, and the fitted results for each shape at each Co composition are represented by a family of dashed lines. The fitted results are summarized in Figure 6d using a Co composition of 35%, which falls within the range of the investigated compositions. Co alloying lowers both volume and surface contributions, suggesting a strong tendency of mixing Co and Pt atoms; however, the dependencies differ with Co−Pt nanoparticle shapes. The fitted enthalpy of mixing and reduction in Pt surface contribution due to Co alloying for each shape of Co−Pt nanoparticle, together with fitted volume and surface contributions in a pure Pt nanoparticle and volume contribution of Co from a bulk calculation, are listed in Table 1.

Over most of the size range, the truncated octahedron is the most stable shape, as it is for pure Pt particles. We can deduce, by extrapolation, that at small particle sizes, (<333 atoms) icosahedron becomes more stable. We infer that this is because the addition of Co in the core switches the order of the surface contribution coefficients for alloyed truncated octahedron

https://doi.org/10.1021/acs.jpcc.3c04639
J. Phys. Chem. C XXXX, XXX, XXX−XXX

(2.512) and icosahedron (2.266) compared to that for pure Pt truncated octahedron (3.213) and icosahedron (3.348), adding that the order of volume contributions remains unchanged for alloyed truncated octahedron (−6.916) and icosahedron (−6.881) versus that in pure Pt truncated octahedron (−6.249) and icosahedron (−6.235), as shown in Figures 5 and 6d. This can be explained by the strain/stress release on the distorted surface of icosahedron when a smaller element such as Co is introduced into the subsurface and core. Specifically, we define the average local strain for a surface atom i as

$$\varepsilon_i = \frac{1}{M}\sum_{j\in \mathrm{NN}_i}\frac{d_{ij}-d_{\mathrm{Pt}}}{d_{\mathrm{Pt}}} \tag{6}$$

where d_{ij} is the interatomic distance between atoms i and j, d_{Pt} is the DFT-calculated lattice constant for an optimized bulk Pt (3.936 Å), NN_i represents the summation over the nearest surface neighbors of atom i, and M is the number of surface neighbors. We calculated the average local strains on the terrace fcc(111) sites for cuboctahedron and icosahedron particles in sizes from 561 to 5083 atoms with and without Co alloying and report the result in Table 2. As we can see, the surface atoms on the cuboctahedron start in compressive strain for pure Pt, and alloying with Co only further compresses the surface atoms. In contrast, the icosahedron starts in tensile strain in the pure system, so alloying with Co allows strain relief and crosses into the compressive regime. As a result, the absolute strain increases with alloying for cuboctahedron and decreases for icosahedron, confirming stress release in icosahedron nanoparticles upon Co alloying.

Table 2. Strain Levels (Engineering Strain, Percent) for Particles in Sizes of 561, 923, 1415, 2057, 2869, 3871, and 5083 Atoms with and without Co Alloying[a]

	cuboctahedron	icosahedron
pure Pt	(−1.321 ± 0.176)%	(+2.333 ± 0.215)%
alloyed	(−3.116 ± 0.068)%	(−1.244 ± 0.190)%

[a]The ± indicates the standard deviation across particle sizes.

If we increase the Co composition to 40%, we found that the crossover between icosahedron and truncated octahedron shifts to a larger size of 570 atoms, further extending the range of stability for icosahedron. Of course, the crossover may also depend on the surrounding environment and surface reactions, which are not considered in this study. Here we mainly aim to provide the physical insights for differences in crossover for Pt and Co−Pt nanoparticles, and the structures used to analyze the crossover for Co−Pt alloy systems can probably be further optimized. The method presented here can readily be extended.

3.4. Order−Disorder Phase Transition in Co−Pt Truncated Octahedrons. Before discussing the order−disorder phase transition, we need to investigate the stable structure of a Co−Pt nanoparticle. Two questions should be answered in this regard—first, is the stable structure ordered? Second, if it is ordered, how? The truncated octahedron structure was chosen for this analysis based on the crossover analysis, as it is the most thermodynamically stable shape for large sizes and is also the structure most commonly reported in experiments.[4,16,59] First, we performed Metropolis simulations at a temperature of 300 K on particles with the composition $Pt_{300}Co_{286}$. We picked a structure after more than 58,600 steps, equivalent to 100 swaps per atom on average, and we treated it as the putative global minima. We relaxed the structure using the force model.

We compared the energy of this structure with its fully ordered $L1_0$ counterpart using both our ML energy model and DFT, using the highly scalable SPARC code. To the best of our knowledge, this DFT validation calculation on a spin-polarized 586-atom structure represents the largest Co−Pt nanoparticle that has been directly validated by a full ab initio method. The shell-by-shell atomic arrangements of both structures are shown in Figure 7. For the ML-found minimum, an alternating preference for Pt and Co atoms can be seen starting with a Pt-rich surface with the subsurface layer fully occupied by Co. Co atoms on the surface of this structure are more likely to occupy terrace fcc(111) sites and to connect with Pt atoms on the surface, consistent with the previous findings in the genetic algorithm study. This observation is validated by aforementioned SPARC DFT calculations to prove that the $L1_0$ ordered Co−Pt truncated octahedron alloy is not the most stable structure but ordered in a different pattern as shown in the configurations in Figure 7a. Both the SPARC DFT calculations and the ML-calculations conclude the Metropolis-derived structure found by ML models is lower in energy than the $L1_0$ structure, with ML predicting 0.097 eV/atom and DFT calculating 0.057 eV/atom. The DFT-maximum atomic forces for the ML-found minimum and $L1_0$ ordered structures are 0.42

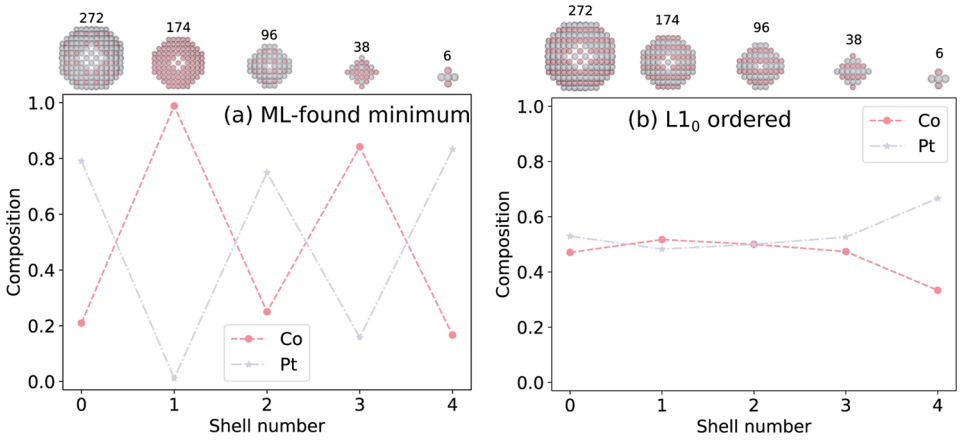

Figure 7. Composition depth profile of a truncated octahedron $Pt_{300}Co_{286}$: the putative global minima found by ML models (a), and the fully $L1_0$ ordered Co−Pt nanoparticle alloy (b). Atomic arrangement at each shell and the total number of atoms are provided at the top.

https://doi.org/10.1021/acs.jpcc.3c04639
J. Phys. Chem. C XXXX, XXX, XXX−XXX

and 0.27 eV/Å, respectively, which are within the ML-predicted maximum atomic uncertainty of forces, 0.43 and 0.42 eV/Å, respectively. Since the Metropolis-found structure has a larger maximum force, we expect its energy may decrease more if it were reoptimized at the DFT level; this would likely have the effect of reducing the energy differences between the ML and DFT estimates. (Performing full relaxations at the DFT level, even with a highly scalable code like SPARC, would be extremely costly due to the scaling of DFT, the spin polarization, and the large number of degrees of freedom in the system). We performed a similar study on the smaller Co−Pt-truncated octahedron $Pt_{96}Co_{105}$, and the comparison between ML predicted putative minima against the $L1_0$ one is included in Figure S7 of Supporting Information.

We also performed Metropolis simulations at a temperature of 500 K on a much larger nanoparticle with 6266 atoms (∼6 nm). We started with a fully $L1_0$ ordered structure, and we wanted to see where the thermodynamic fluctuations lead the structure. We took out a structure after 330,000 steps, showing the configuration for each shell in Figure 8. It is clear that the first

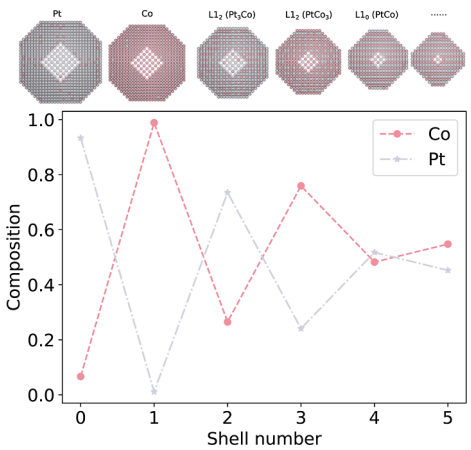

Figure 8. Depth profile of compositions and configurations at each shell for 6 nm $Co_{3102}Pt_{3164}$ optimized by Metropolis Monte Carlo simulations.

four outermost shells change to a distinct orderliness, whereas we find an almost unchanged $L1_0$-like structure going from the fifth shell to the center of the truncated octahedron. Interestingly, the optimized structure for a truncated octahedron with nearly equal compositions of Pt and Co follows a pattern of atomic arrangement as

$$\mathrm{Pt} \rightarrow \mathrm{Co} \rightarrow L1_2(\mathrm{Pt_3Co}) \rightarrow L1_2(\mathrm{PtCo_3}) \rightarrow L1_0(\mathrm{PtCo}) \rightarrow \cdots \rightarrow L1_0(\mathrm{PtCo})$$

So far, we can conclude that the optimal particle for a truncated octahedron with equal compositions displays concentric Pt and Co shells at the outermost two shells, then respective Pt-rich and Co-rich $L1_2$ ordered at the third and fourth shell, and fully $L1_0$ ordered close to the center.

To find the temperature for the order−disorder phase transition, we carried out a series of Metropolis simulations at various temperatures. We studied the order−disorder phase transition for two structures; one is a 500-atom bulk cell $Pt_{250}Co_{250}$ and the other is a 1289-atom truncated octahedron $Pt_{632}Co_{657}$. We employed a long-range order (LRO) parameter (Φ) introduced by Cowley[60] to describe the order−disorder transition, and it takes the form of

$$\Phi = \max_{i \in \{x,y,z\}} (\{\Phi_i\})$$
$$\text{where}\ \Phi_i = |p_{A,i} - 1/2| + |p_{B,i} - 1/2| \quad (7)$$

where $p_{A,i}$ and $p_{B,i}$ are the occupation probabilities on each sublattice of the $L1_0$ phase evaluated in an ordering direction i. As the stable structure of truncated octahedron found at 300 K is similar to that of the aforementioned 6266-atom structure, only exhibiting $L1_0$ ordering from the fifth shell to the center, we only consider those $L1_0$ ordered shells for the order−disorder transition in the 3.3 nm truncated octahedron nanoparticle $Pt_{632}Co_{657}$. Figure 9 shows the order parameters calculated at

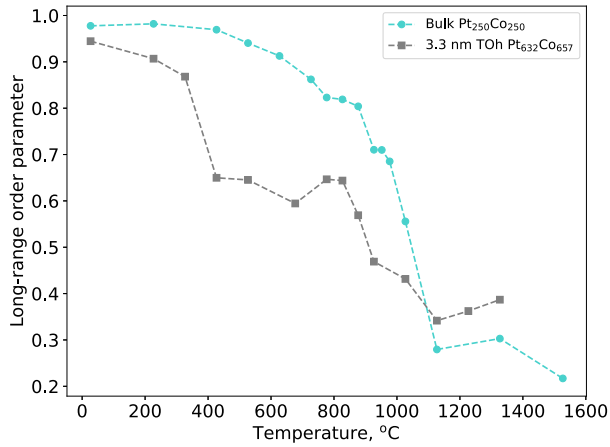

Figure 9. Long-range order parameter for a 500-atom bulk cell and a 1289-atom 3.3 nm truncated octahedron calculated by Metropolis simulations at various temperatures. TOh is short for a truncated octahedron.

various temperatures by Metropolis simulations on a bulk cell and a nanoparticle. Although there is not a sharp phase transition, we can see that the loss of order occurs in the vicinity of the experimentally observed transition temperature of ∼850 °C,[61,62] although our calculations appear to predict it to be slightly higher at a temperature of ∼1050 °C. This deviation is similar to what has been found by well-validated empirical interatomic potentials.[14] For the 1289-atom truncated octahedron, there exists a much smoother transition region where the transition temperature is found to be around 900 °C, which is 150 °C lower than that of a bulk. The size effect agrees well with experimental observations and simulations in the work of Alloyeau et al.,[14] in which order−disorder phase transition temperature is lowered by at least 175 °C. This phenomenon can be understood by the surface induced disordering due to the reduced coordination hence an overall lowered order−disorder transition temperature.[12]

4. CONCLUSIONS

Based on an NFT approach, robust neural network models have been developed for Co−Pt nanoparticles of up to several thousand atoms in size, using training sets containing images with no more than 168 atoms/image. This work also demonstrates that the NFT approach is applicable to multielement magnetic nanoparticles. The resulting models can readily be improved by addressing uncertain local chemical environ-

https://doi.org/10.1021/acs.jpcc.3c04639
J. Phys. Chem. C XXXX, XXX, XXX−XXX

ments when necessary. By pairing these models with genetic algorithms and Metropolis Monte Carlo simulations, we have presented a thorough study of the stable structures of Co−Pt nanoparticles. We summarize the key findings below, which not only refine existing understandings of the thermodynamic stability of Co−Pt nanoparticles but also offer guidelines for the synthesis of nanoparticle catalysts in experiments. The experimental guidelines include, but are not limited to, using temperature to control the orderliness of the nanoparticle and tuning surface energy with a capping agent targeting desired nanoparticle shapes.

1. Co−Pt nanoparticles exhibit a strong tendency to form alternating layers near the surface, with a platinum-rich skin and a cobalt-rich underlayer. This was seen in many systems throughout this study, and the concentric nature continued through the fourth shell in the case of a 6 nm (6266-atom) structure.
2. Co−Pt fcc(100) surfaces also exhibit a strong tendency to form an $L1_0$ ordered structure featuring alternating Pt and Co layers. Co−Pt fcc(111) surfaces show more flexibility of the atomic arrangement while the major feature is also the alternating layers.
3. The truncated octahedron is the most stable shape for Pt nanoparticles of moderate to large sizes (200−7000 atoms), due to its low surface and volume energies. This explains its frequent appearance in experiments. The stability of icosahedron and cuboctahedron particles is always less, but these two shapes exhibit a crossover in stability at a size of ∼500 atoms.
4. The truncated octahedron is the most stable shape for large Co−Pt nanoparticles, while the icosahedron is more stable for smaller nanoparticles. An composition-dependent empirical model was introduced to study the crossover among structural motifs in Co−Pt nanoparticles. The addition of Co improves the stability of icosahedron, leading to a crossover between icosahedron and truncated octahedron at the size of ∼333 atoms for a given Co composition of 35%. It can be rationalized by the significant stress release on the distorted fcc(111) surfaces of icosahedron when a smaller element is introduced in the core. The crossover moves to a larger size when more Co atoms are added.
5. Metropolis simulations reveal that the most stable atomic arrangement of a Co−Pt truncated octahedron with nearly equal Co and Pt compositions is not fully $L1_0$ ordered, as often found by well-parametrized empirical potentials. Instead, it displays a more complex pattern going from the outermost shell to the center of truncated octahedron, which is confirmed by large-scale DFT calculations on SPARC. The outermost shell is Pt segregated, followed by a Pt depleted second shell. The third and fourth shells are $L1_2$-like structures rich in Pt and Co, respectively. Deeper shells all exhibit $L1_0$-like atomic arrangement.
6. The order−disorder phase transition for a bulk and nanoparticle has been studied based on a long-range order parameter. Nanoparticles show a lower transition temperature and a much smoother transition compared to a bulk Co−Pt alloy.
7. The energy convex hull for a 147-atom Co−Pt icosahedron constructed by neural network models is quantitatively accurate compared to brute-force ab initio calculations, and a new low-energy atomic arrangement for $Pt_{80}Co_{67}$ is identified.

■ ASSOCIATED CONTENT

Data Availability Statement

Supporting data and code to reproduce some simulation results can be found here: https://github.com/cengc13/nft-copt-NP-structures.

Supporting Information

The Supporting Information is available free of charge at https://pubs.acs.org/doi/10.1021/acs.jpcc.3c04639.

Representative cuboctahedron and icosahedron structures used to generate the training data (atomic chunks) and the corresponding average atomic uncertainties for the relaxed structures of those full-size nanoparticles, statistics for the atomic chunks, validation of force consistency between GPAW and SPARC, energies and configurations for a 147-atom icosahedron and cuboctahedron, energies and configurations for two $Pt_{80}Co_{67}$ icosahedra, fitted size dependency of pure Pt nanoparticle energies including edge terms, and shell-by-shell compositions and configurations of a $Pt_{96}Co_{105}$ truncated octahedron (PDF)

■ AUTHOR INFORMATION

Corresponding Author

Andrew A. Peterson − *School of Engineering, Brown University, Providence, Rhode Island 02912, United States;* orcid.org/0000-0003-2855-9482; Phone: +1 401-863-2153; Email: andrew_peterson@brown.edu

Authors

Cheng Zeng − *School of Engineering, Brown University, Providence, Rhode Island 02912, United States;* orcid.org/0000-0002-1296-913X

Sushree Jagriti Sahoo − *School of Chemical and Biomolecular Engineering, Georgia Institute of Technology, Atlanta, Georgia 30318, United States*

Andrew J. Medford − *School of Chemical and Biomolecular Engineering, Georgia Institute of Technology, Atlanta, Georgia 30318, United States;* orcid.org/0000-0001-8311-9581

Complete contact information is available at: https://pubs.acs.org/10.1021/acs.jpcc.3c04639

Notes

The authors declare no competing financial interest.

■ ACKNOWLEDGMENTS

The authors thank Phanish Suryanarayana and Qimen Xu for their support in running the SPARC code and providing feedback on convergence issues. This work was supported by the U.S. Department of Energy's Basic Energy Science, Computational Chemical Sciences Program Office, under award no. DE-SC0019441. Cheng Zeng acknowledges support from the Presidential Fellowship at Brown University. This work was undertaken using the computational resources at the Brown University Center for Computation and Visualization (CCV).

■ REFERENCES

(1) Ristau, R. A.; Barmak, K.; Lewis, L. H.; Coffey, K. R.; Howard, J. K. On the relationship of high coercivity and L1 ordered phase in CoPt and FePt thin films. *J. Appl. Phys.* **1999**, *86*, 4527−4533.

(2) Sun, S.; Murray, C. B.; Weller, D.; Folks, L.; Moser, A. Monodisperse FePt Nanoparticles and Ferromagnetic FePt Nanocrystal Superlattices. *Science* **2000**, *287*, 1989−1992.
(3) Ferrando, R.; Jellinek, J.; Johnston, R. L. Nanoalloys: From Theory to Applications of Alloy Clusters and Nanoparticles. *Chem. Rev.* **2008**, *108*, 845−910.
(4) Li, J.; Sharma, S.; Wei, K.; Chen, Z.; Morris, D.; Lin, H.; Zeng, C.; Chi, M.; Yin, Z.; Muzzio, M.; Shen, M.; Zhang, P.; Peterson, A. A.; Sun, S. Anisotropic Strain Tuning of L10 Ternary Nanoparticles for Oxygen Reduction. *J. Am. Chem. Soc.* **2020**, *142*, 19209−19216.
(5) Sun, X.; Huang, Y.; Nikles, D. E. FePt and CoPt magnetic nanoparticles film for future high density data storage media. *Int. J. Nanotechnol.* **2004**, *1*, 328−346.
(6) Jun, Y. W.; Choi, J. S.; Cheon, J. Heterostructured magnetic nanoparticles: their versatility and high performance capabilities. *Chem. Commun.* **2007**, *12*, 1203−1214.
(7) Christodoulides, J. A.; Huang, Y.; Zhang, Y.; Hadjipanayis, G. C.; Panagiotopoulos, I.; Niarchos, D. CoPt and FePt thin films for high density recording media. *J. Appl. Phys.* **2000**, *87*, 6938−6940.
(8) Yoshida, T.; Kojima, K. Toyota MIRAI Fuel Cell Vehicle and Progress Toward a Future Hydrogen Society. *Electrochem. Soc. Interface* **2015**, *24*, 45−49.
(9) Wang, C.; Spendelow, J. S. Recent developments in Pt−Co catalysts for proton-exchange membrane fuel cells. *Curr. Opin. Electrochem.* **2021**, *28*, 100715.
(10) Mehaddene, T.; Kentzinger, E.; Hennion, B.; Tanaka, K.; Numakura, H.; Marty, A.; Parasote, V.; Cadeville, M. C.; Zemirli, M.; Pierron-Bohnes, V. Lattice dynamics and migration enthalpies in CoPt3 and FePd. *Phys. Rev. B* **2004**, *69*, 024304.
(11) Andreazza, P.; Pierron-Bohnes, V.; Tournus, F.; Andreazza-Vignolle, C.; Dupuis, V. Structure and order in cobalt/platinum-type nanoalloys: from thin films to supported clusters. *Surf. Sci. Rep.* **2015**, *70*, 188−258.
(12) Yang, B.; Asta, M.; Mryasov, O. N.; Klemmer, T. J.; Chantrell, R. W. The nature of A1−L10 ordering transitions in alloy nanoparticles: A Monte Carlo study. *Acta Mater.* **2006**, *54*, 4201−4211.
(13) Müller, M.; Albe, K. Lattice Monte Carlo simulations of FePt nanoparticles: Influence of size, composition, and surface segregation on order-disorder phenomena. *Phys. Rev. B* **2005**, *72*, 094203.
(14) Alloyeau, D.; Ricolleau, C.; Mottet, C.; Oikawa, T.; Langlois, C.; Le Bouar, Y.; Braidy, N.; Loiseau, A. Size and shape effects on the order−disorder phase transition in CoPt nanoparticles. *Nat. Mater.* **2009**, *8*, 940−946.
(15) He, D. S.; He, D.; Wang, J.; Lin, Y.; Yin, P.; Hong, X.; Wu, Y.; Li, Y. Ultrathin Icosahedral Pt-Enriched Nanocage with Excellent Oxygen Reduction Reaction Activity. *J. Am. Chem. Soc.* **2016**, *138*, 1494−1497.
(16) Xia, Y.; Xiong, Y.; Lim, B.; Skrabalak, S. E. Shape-Controlled Synthesis of Metal Nanocrystals: Simple Chemistry Meets Complex Physics? *Angew. Chem., Int. Ed.* **2009**, *48*, 60−103.
(17) Wu, J.; Qi, L.; You, H.; Gross, A.; Li, J.; Yang, H. Icosahedral Platinum Alloy Nanocrystals with Enhanced Electrocatalytic Activities. *J. Am. Chem. Soc.* **2012**, *134*, 11880−11883.
(18) Shao, M.; Peles, A.; Shoemaker, K. Electrocatalysis on Platinum Nanoparticles: Particle Size Effect on Oxygen Reduction Reaction Activity. *Nano Lett.* **2011**, *11*, 3714−3719.
(19) Ahmadi, T. S.; Wang, Z. L.; Green, T. C.; Henglein, A.; El-Sayed, M. A. Shape-Controlled Synthesis of Colloidal Platinum Nanoparticles. *Science* **1996**, *272*, 1924−1925.
(20) Mackay, A. L. A dense non-crystallographic packing of equal spheres. *Acta Crystallogr.* **1962**, *15*, 916−918.
(21) Cleveland, C. L.; Landman, U. The energetics and structure of nickel clusters: Size dependence. *J. Chem. Phys.* **1991**, *94*, 7376−7396.
(22) Uppenbrink, J.; Wales, D. J. Structure and energetics of model metal clusters. *J. Chem. Phys.* **1992**, *96*, 8520−8534.
(23) Baletto, F.; Ferrando, R.; Fortunelli, A.; Montalenti, F.; Mottet, C. Crossover among structural motifs in transition and noble-metal clusters. *J. Chem. Phys.* **2002**, *116*, 3856−3863.
(24) Nishioka, K. Thermodynamics of a liquid microcluster. *Phys. Rev. A* **1977**, *16*, 2143−2152.
(25) Northby, J. A.; Xie, J.; Freeman, D. L.; Doll, J. D. Binding energy of large icosahedral and cuboctahedral Lennard-Jones clusters. *Z. Physik D Atoms, Mol. Clust.* **1989**, *12*, 69−71.
(26) Zhu, B.; Guesmi, H.; Creuze, J.; Legrand, B.; Mottet, C. Crossover among structural motifs in Pd−Au nanoalloys. *Phys. Chem. Chem. Phys.* **2015**, *17*, 28129−28136.
(27) Behler, J.; Parrinello, M. Generalized Neural-Network Representation of High-Dimensional Potential-Energy Surfaces. *Phys. Rev. Lett.* **2007**, *98*, 146401.
(28) Bartók, A. P.; Payne, M. C.; Kondor, R.; Csányi, G. Gaussian Approximation Potentials: the accuracy of quantum mechanics, without the electrons. *Phys. Rev. Lett.* **2010**, *104*, 136403.
(29) Rupp, M.; Tkatchenko, A.; Müller, K. R.; von Lilienfeld, O. A. Fast and Accurate Modeling of Molecular Atomization Energies with Machine Learning. *Phys. Rev. Lett.* **2012**, *108*, 058301.
(30) Behler, J. Four Generations of High-Dimensional Neural Network Potentials. *Chem. Rev.* **2021**, *121*, 10037−10072.
(31) Deringer, V. L.; Bartók, A. P.; Bernstein, N.; Wilkins, D. M.; Ceriotti, M.; Csányi, G. Gaussian Process Regression for Materials and Molecules. *Chem. Rev.* **2021**, *121*, 10073−10141.
(32) Unke, O. T.; Chmiela, S.; Sauceda, H. E.; Gastegger, M.; Poltavsky, I.; Schütt, K. T.; Tkatchenko, A.; Müller, K. R. Machine Learning Force Fields. *Chem. Rev.* **2021**, *121*, 10142−10186.
(33) Botu, V.; Batra, R.; Chapman, J.; Ramprasad, R. Machine Learning Force Fields: Construction, Validation, and Outlook. *J. Phys. Chem. C* **2017**, *121*, 511−522.
(34) Zeng, C.; Chen, X.; Peterson, A. A. A nearsighted force-training approach to systematically generate training data for the machine learning of large atomic structures. *J. Chem. Phys.* **2022**, *156*, 064104.
(35) Peterson, A. A.; Christensen, R.; Khorshidi, A. Addressing uncertainty in atomistic machine learning. *Phys. Chem. Chem. Phys.* **2017**, *19*, 10978−10985.
(36) Khorshidi, A.; Peterson, A. A. Amp: A modular approach to machine learning in atomistic simulations. *Comput. Phys. Commun.* **2016**, *207*, 310−324.
(37) Singraber, A.; Behler, J.; Dellago, C. Library-Based LAMMPS Implementation of High-Dimensional Neural Network Potentials. *J. Chem. Theory Comput.* **2019**, *15*, 1827−1840.
(38) Lee, K.; Yoo, D.; Jeong, W.; Han, S. SIMPLE-NN: An efficient package for training and executing neural-network interatomic potentials. *Comput. Phys. Commun.* **2019**, *242*, 95−103.
(39) Shuaibi, M.; Hu, Y.; Lei, X.; Comer, B. M.; Adams, M.; Paras, J.; Chen, R. Q.; Musa, E.; Musielewicz, J.; Peterson, A. A.; Medford, A. J.; Ulissi, Z. AmpTorch: A Python package for scalable fingerprint-based neural network training on multi-element systems with integrated uncertainty quantification. *J. Open Source Softw.* **2023**, *8*, 5035.
(40) Enkovaara, J.; Rostgaard, C.; Mortensen, J. J.; Chen, J.; Dułak, M.; Ferrighi, L.; Gavnholt, J.; Glinsvad, C.; Haikola, V.; Hansen, H. A.; et al. Electronic structure calculations with GPAW: a real-space implementation of the projector augmented-wave method. *J. Phys.: Condens. Matter* **2010**, *22*, 253202.
(41) Perdew, J. P.; Burke, K.; Ernzerhof, M. Generalized Gradient Approximation Made Simple. *Phys. Rev. Lett.* **1996**, *77*, 3865−3868.
(42) Xu, Q.; Sharma, A.; Comer, B.; Huang, H.; Chow, E.; Medford, A. J.; Pask, J. E.; Suryanarayana, P. SPARC: Simulation Package for Ab-initio Real-space Calculations. *SoftwareX* **2021**, *15*, 100709.
(43) Ghosh, S.; Suryanarayana, P. SPARC: Accurate and efficient finite-difference formulation and parallel implementation of Density Functional Theory: Isolated clusters. *Comput. Phys. Commun.* **2017**, *212*, 189−204.
(44) Ghosh, S.; Suryanarayana, P. SPARC: Accurate and efficient finite-difference formulation and parallel implementation of Density Functional Theory: Extended systems. *Comput. Phys. Commun.* **2017**, *216*, 109−125.
(45) van Setten, M. J.; Giantomassi, M.; Bousquet, E.; Verstraete, M. J.; Hamann, D. R.; Gonze, X.; Rignanese, G. M. The PseudoDojo: Training and grading a 85 element optimized norm-conserving pseudopotential table. *Comput. Phys. Commun.* **2018**, *226*, 39−54.

https://doi.org/10.1021/acs.jpcc.3c04639
J. Phys. Chem. C XXXX, XXX, XXX−XXX

(46) Deaven, D. M.; Ho, K. M. Molecular Geometry Optimization with a Genetic Algorithm. *Phys. Rev. Lett.* **1995**, *75*, 288−291.
(47) Johnston, R. L. Evolving better nanoparticles: Genetic algorithms for optimising cluster geometries. *Dalton Trans.* **2003**, *22*, 4193−4207.
(48) Vilhelmsen, L. B.; Hammer, B. Systematic Study of Au_6 to Au_{12} Gold Clusters on MgO(100) *F* Centers Using Density-Functional Theory. *Phys. Rev. Lett.* **2012**, *108*, 126101.
(49) Lysgaard, S.; Landis, D. D.; Bligaard, T.; Vegge, T. Genetic Algorithm Procreation Operators for Alloy Nanoparticle Catalysts. *Top. Catal.* **2014**, *57*, 33−39.
(50) Van den Bossche, M.; Grönbeck, H.; Hammer, B. Tight-Binding Approximation-Enhanced Global Optimization. *J. Chem. Theory Comput.* **2018**, *14*, 2797−2807.
(51) Hjorth Larsen, A.; Jørgen Mortensen, J.; Blomqvist, J.; Castelli, I.; Christensen, R.; Dułak, M.; Friis, J.; Groves, M.; Hammer, B.; Hargus, C.; et al. The atomic simulation environment - A python library for working with atoms. *J. Phys.: Condens.Matter* **2017**, *29*, 273002.
(52) Boes, J. R.; Kitchin, J. R. Modeling Segregation on AuPd(111) Surfaces with Density Functional Theory and Monte Carlo Simulations. *J. Phys. Chem. C* **2017**, *121*, 3479−3487.
(53) Gruner, M. E.; Rollmann, G.; Entel, P.; Farle, M. Multiply Twinned Morphologies of FePt and CoPt Nanoparticles. *Phys. Rev. Lett.* **2008**, *100*, 087203.
(54) Oriani, R.; Murphy, W. K. Thermodynamics of ordering alloys-IV heats of formation of some alloys of transition metals. *Acta Metall.* **1962**, *10*, 879−885.
(55) Noh, S. H.; Seo, M. H.; Seo, J. K.; Fischer, P.; Han, B. First principles computational study on the electrochemical stability of Pt−Co nanocatalysts. *Nanoscale* **2013**, *5*, 8625−8633.
(56) Baletto, F.; Ferrando, R. Structural properties of nanoclusters: Energetic, thermodynamic, and kinetic effects. *Rev. Mod. Phys.* **2005**, *77*, 371−423.
(57) Tang, L.; Han, B.; Persson, K.; Friesen, C.; He, T.; Sieradzki, K.; Ceder, G. Electrochemical Stability of Nanometer-Scale Pt Particles in Acidic Environments. *J. Am. Chem. Soc.* **2010**, *132*, 596−600.
(58) Wang, X.; Vara, M.; Luo, M.; Huang, H.; Ruditskiy, A.; Park, J.; Bao, S.; Liu, J.; Howe, J.; Chi, M.; et al. Pd@Pt Core−Shell Concave Decahedra: A Class of Catalysts for the Oxygen Reduction Reaction with Enhanced Activity and Durability. *J. Am. Chem. Soc.* **2015**, *137*, 15036−15042.
(59) Li, J.; Sun, S. Intermetallic Nanoparticles: Synthetic Control and Their Enhanced Electrocatalysis. *Acc. Chem. Res.* **2019**, *52*, 2015−2025.
(60) Cowley, J. M. Short- and Long-Range Order Parameters in Disordered Solid Solutions. *Phys. Rev.* **1960**, *120*, 1648−1657.
(61) Leroux, C.; Cadeville, M. C.; Pierron-Bohnes, V.; Inden, G.; Hinz, F. Comparative investigation of structural and transport properties of L10-NiPt and CoPt phases: the role of magnetism. *J. Phys. F: Met. Phys.* **1988**, *18*, 2033−2051.
(62) Le Bouar, Y.; Loiseau, A.; Finel, A. Origin of the complex wetting behavior in Co-Pt alloys. *Phys. Rev. B* **2003**, *68*, 224203.

https://doi.org/10.1021/acs.jpcc.3c04639
J. Phys. Chem. C XXXX, XXX, XXX−XXX